bioRxiv preprint doi: https://doi.org/10.1101/166413; this version posted July 21, 2017. The copyright holder for this preprint (which was not certified by peer review) is the author/funder, who has granted bioRxiv a license to display the preprint in perpetuity. It is made available under aCC-BY-NC-ND 4.0 International license.

Decision and navigation in mouse parietal cortex

Michael Krumin[1], Kenneth D Harris[2], and Matteo Carandini[1]

1, UCL Institute of Ophthalmology, University College London, London EC1V 9EL, United Kingdom
2, UCL Institute of Neurology, University College London, London WC1E 6DE, United Kingdom

Posterior parietal cortex (PPC) has been involved in controlling body movement and navigation, and in making decisions based on vision. To evaluate these views, we measured PPC activity while mice performed a visual decision task by virtual navigation. We discovered that PPC neurons are selective for specific combinations of the animal's position in the environment and of its heading angle. This selectivity closely predicted the activity of PPC cells, including their apparent selectivity for the mouse's decision and the arrangement of their firing patterns in sequences, both of which simply reflected the influence on PPC of the animal's navigation trajectory. Alternative models based on visual or motor variables were not as successful. We conclude that when mice use vision to make spatial choices, parietal cortex encodes navigational attributes such as position and heading rather than decisions.

Introduction

Posterior parietal cortex (PPC) is recognized as a key nexus of sensorimotor integration (Milner and Goodale, 2006), yet there are discordant views as to its function.

Classical studies in primates related PPC activity to the control of body movement (Andersen and Buneo, 2002; Andersen and Cui, 2009; Andersen and Mountcastle, 1983; Bisley and Goldberg, 2010; Cohen and Andersen, 2002; Park et al., 2014). For instance, some neurons in monkey PPC are influenced by movements of eyes, head, limbs, and body (Cohen and Andersen, 2002), by the intention to execute such movements (Andersen and Buneo, 2002), or by the attention devoted to the resulting position (Bisley and Goldberg, 2010).

A complementary set of studies performed in rodents suggested an important role of PPC in spatial navigation (McNaughton et al., 1994; Nitz, 2006, 2012; Save and Poucet, 2000, 2009; Whitlock et al., 2012; Wilber et al., 2014). Rat PPC encodes combinations of spatial location and body movement (McNaughton et al., 1994; Nitz, 2006, 2012; Whitlock et al., 2012; Wilber et al., 2014). Inactivating it, moreover, can impair navigation (Save and Poucet, 2000, 2009).

Another body of experiments, performed both in primates and in rodents, indicated a role of PPC in decision making, especially for decisions based on vision (Andersen and Cui, 2009; Erlich et al., 2015; Goard et al., 2016; Gold and Shadlen, 2007; Katz et al., 2016; Latimer et al., 2015; Licata et al., 2017; Platt and Glimcher, 1999; Raposo et al., 2014; Sugrue et al., 2004). Studies in rodents found decision signals to be widespread in PPC populations, where they are mixed with other signals (Goard et al., 2016; Raposo et al., 2014). One study, in particular, found decision signals to be remarkably common: each PPC neuron fires only for a particular decision and only at a particular moment in a stereotyped sequence (Harvey et al., 2012).

In principle, all these views could be correct. However, this is hard to establish from existing studies. In reality, moreover, the relevant factors are hard to separate. For instance, decisions often result in navigation, and navigation involves a myriad decisions. Similarly, in any condition other than complete darkness, head movement influences vision,

bioRxiv preprint doi: https://doi.org/10.1101/166413; this version posted July 21, 2017. The copyright holder for this preprint (which was not certified by peer review) is the author/funder, who has granted bioRxiv a license to display the preprint in perpetuity. It is made available under aCC-BY-NC-ND 4.0 International license.

and vision in turn guides head and body movements.

To investigate how spatial function, body movement, and decision-making are reflected in PPC activity, we took advantage of the capabilities allowed by virtual reality. We trained mice in a task that engages both visual decision-making and navigation through an environment. During this task, we recorded from populations of PPC neurons and asked whether their activity encodes navigation, decision-making, or both.

As described below, the results came out strongly in favor of one view: we found that parietal neurons carry powerful spatial signals, but found no evidence that on top of those signals there are any signals related to decision. Indeed, taking into account the spatial preferences of the neurons and the trajectories taken by the mouse, we could predict the precise pattern of activation of individual neurons.

In particular, our observations closely replicated the apparent selectivity of PPC activity on choice, including the arrangement of PPC neurons in sequences of activation (Harvey et al., 2012). However, we could explain these observations parsimoniously by the effect on PPC neurons of two simple navigational parameters: position in the environment and heading. These two parameters predicted the activity of PPC neurons, better than descriptions based on body movement, on visual processing, or on decision. These results bridge hitherto separate views of parietal cortical function, and point to a synthesis of these views.

Results

To evaluate these views, we measured, modeled, and decoded the activity of large populations of PPC neurons while mice reported perceptual decisions by navigating in virtual reality (Figure 1**a**-**c**). Head-fixed mice performed a visual two-alternative forced-choice (2AFC) contrast-detection task by walking on an air-suspended ball (Dombeck et al., 2010) (Figure 1**a**, Suppl. Movie 1). Mice traversed a virtual corridor where one of the side walls contained a vertical grating, and indicated that side by turning into the left or right arms of the T-maze (Figure 1**b**). Grating contrast and side varied randomly across trials. A water reward was delivered on successful trials, and a brief white noise sound on unsuccessful trials. Mice learned this task to high proficiency, and their performance exhibited a lawful dependence on contrast (Figure 1**c**).

The decisions of the animal were typically evident before the mouse reached the end of the T-maze, as the mice turned towards the intended side before reaching the end of the corridor (Figure 1**d**-**h**). To describe the navigation paths, we considered two variables: position along the corridor (z) and heading angle (θ). In these coordinates, the paths that ended in left and right choices progressively deviated from each other: the animal started heading towards the chosen side before reaching the end of the corridor. This dependence of heading angle θ on decision was particularly clear for easier trials, i.e. trials with higher contrast (Figure 1**d**-**f**). The final choice could thus be predicted from the heading angle with increasing accuracy as the mouse reached the end of the corridor (Figure 1**g**,**h**).

We measured PPC population activity in this task using 2-photon calcium imaging (Figure 1**i**,**j**). To identify the borders of visual cortical areas we obtained retinotopic maps using widefield imaging (Figure 1**i**), and identified PPC as a region anterior to the V1 region, along a contour of pixels that represent a retinotopic azimuth of 60-80 degrees. The average stereotaxic coordinates of this region were close to the coordinates used in previous studies (-2.0 mm AP, 1.7 mm ML, Harvey et al., 2012), as shown in Suppl. Figure 1. We then targeted 2-photon imaging to PPC while the mouse was performing the task (Figure 1**j**). We then applied *Suite2p*, an image-processing pipeline that provides image registration, cell detection, and neuropil correction, to obtain calcium traces from well-isolated neurons (Pachitariu et al., 2016).

bioRxiv preprint doi: https://doi.org/10.1101/166413; this version posted July 21, 2017. The copyright holder for this preprint (which was not certified by peer review) is the author/funder, who has granted bioRxiv a license to display the preprint in perpetuity. It is made available under aCC-BY-NC-ND 4.0 International license.

In agreement with previous observations in a memory-based task (Harvey et al., 2012), all the recorded PPC cells could be divided into two groups forming distinct, choice-dependent sequences of activation (Figure 1**k**-**n**). One group of cells responded primarily during trials that ended in a leftward choice (Figure 1**k**,**l**), and the other during trials that ended in a rightward choice (Figure 1**m**,**n**). Moreover, cells could be ordered based on their firing during the performance of the task, so that the responses of each group of cells could be arranged in a sequence of activations (Harvey et al., 2012). While cells that responded during the initial part of the task tended to fire in both trials that ended with left and right choices, the rest of the cells unambiguously fired only in one or the other of those trials.

This apparent dependence on choice, however, could be explained by a dependence of PPC firing on the animal's position and heading (Figure 2). For example, consider a PPC neuron that typically fired in the late part of trials, and almost exclusively when the trials ended in a rightward choice (Figure 2**a**,**b**). If we plot the density of this neuron's calcium activity as a function of position z and heading θ, we find that the firing defined a clear response field (Figure 2**e**). This "position-heading field" was sufficient to accurately predict the calcium activity of the cell as a function of time (Figure 2**f,g**), capturing not only the overall preference for trajectories that ended in rightward choices (Figure 2**c**), but also detailed differences in responses in individual trials (Figure 2**d**). Indeed, the model correctly predicted that the cell would occasionally respond during trials ended in leftward choices (for positive contrasts, traces above the black bar in Figure 2**b,c**).

The high quality of these predictions was common in the PPC population (Figure 2**h-k**). The correlation between model predictions and calcium traces was 0.44 ± 0.16 (median ± m.a.d., n = 1,922 cells). High correlation was not associated with a particular preference for position or heading: cells whose responses were accurately predicted could have a variety of position-heading fields (Figure 2**h-j**). For all these cells, the model performed well in describing the trial-by-trial variations in activity (Suppl. Figure 2).

Position-heading fields were sufficient to explain the arrangement of PPC responses in choice-dependent sequences. Just as we had done for the example cell (Figure 2**c**), for each PPC neuron we predicted responses for all trials and averaged these predictions depending on whether the trials ended in rightward choices or leftward choices (Figure 3**a**). The resulting predictions describe orderly, choice-dependent sequences of activation, which replicate the essential features of those seen in the data (Figure 1**k**-**n**). Choice-dependent sequences of activation thus seem to emerge because of a combination of two factors: the fact that mice take different trajectories in trials that end with leftward vs. rightward choices (Figure 1**d-f**), and the fact that different PPC cells prefer different combinations of position and heading (Figure 2h-j).

One way in which PPC cells could predict choice, therefore, is simply through their preferred heading: cells with preferred leftward heading are more likely to fire when the animal heads leftward, i.e. when the animal will ultimately choose the left arm. This is precisely what we observed: cells that responded preferentially in trials ending in leftward choices almost invariably preferred negative (leftward) heading values, and the same was true for rightward choices and positive (rightward) heading values (Figure 3**b**).

The success of the position-heading model raises the question of whether in this task PPC neurons actually carry any decision signals beyond those already embodied in the animal's trajectory. To test this, we contrasted the success of the position-heading model with a sequence of alternatives which explicitly included the animal's decisions, and evaluated their ability to predict cell firing using 10-fold cross-validation, where 90% of the data

bioRxiv preprint doi: https://doi.org/10.1101/166413; this version posted July 21, 2017. The copyright holder for this preprint (which was not certified by peer review) is the author/funder, who has granted bioRxiv a license to display the preprint in perpetuity. It is made available under aCC-BY-NC-ND 4.0 International license.

is used for training and 10% cross-validation (Figure 3**c-e**). In the first alternative model, responses depend on position along the track (*z*) and a binary decision variable (*d*), but not heading direction (θ). This position-decision model is implicit in the graphs that describe choice-selective sequences of activation (Harvey et al., 2012) (Figure 1**k**). On a cell-by-cell basis, the position-decision model did markedly worse than the position-heading model (Figure 3**c**). Cross-validation ensures that this result is not due to different numbers of parameters (there are multiple possible headings, vs. only two possible decisions). The second alternative model extends the position-heading model to also include knowledge of the mouse decisions. This model performed worse: predictions based on position and heading alone tended to be more accurate (Figure 3**d**). The additional parameter is penalized by cross-validation, indicating that it is unnecessary. The importance of heading in predicting responses is further confirmed by comparing predictions of the two alternative models: the model that includes heading is invariably more accurate than the model that does not (Figure 3**e**). We therefore conclude that the mouse's heading direction is a better predictor of PPC responses than the mouse's decision, and that once heading direction is known, the mouse's decision provides no additional predictability of PPC firing.

The PPC neurons recorded within each session differed in their position-heading fields, and as a population they tended to tile the whole z-θ space (Figure 4**a**). We therefore asked if PPC population activity was sufficient to decode the mouse's trajectory through virtual space. A simple Bayesian decoder (Oram et al., 1998; Zhang et al., 1998) (Suppl. Figure 3) successfully predicted the position of the animal in z-θ as a function of time (Figure 4**b**) and throughout the trajectory (Figure 4**c;** Suppl. Movie 2). In predicting the final choice, decoding the population was just as good as observing the animal's actual heading: both showed a similar dependence on position z (Figure 4**d**) and stimulus contrast (Figure 4**e**).

Taken together, these results suggest that the activity of PPC neurons in our task largely reflects two spatial attributes: position and heading. A possible caveat in this conclusion, however, is that in our experiment those spatial attributes may covary with visual and motor factors. Position and heading determined the visual scene, and the visual scene could in turn drive the activity of PPC neurons, especially given that mouse PPC overlaps at least partially with regions of higher visual cortex (Wang and Burkhalter, 2007; Zhuang et al., 2017). Likewise, position in z-θ space is itself determined by the animal's movement on the ball and therefore by the time courses of motor factors such as linear and angular velocity, which may in turn determine PPC activity (McNaughton et al., 1994; Nitz, 2006; Whitlock, 2014; Whitlock et al., 2012).

To assess the role of visual factors, we ran a control experiment in open loop, where the animal passively viewed a replay of visual scenes presented in previous task trials. In this open-loop condition only a minority of PPC neurons maintained their preferences for position and heading, and even in those neurons the responses were much weaker (Suppl. Figure 4**a**). Moreover, for the majority of PPC cells, the activity in the open-loop condition was not predictable from the preferences for position and heading estimated during the task. This is perhaps remarkable, given that parietal areas of the mouse cortex (Kirkcaldie, 2012) are generally considered to overlap with visual areas such as RL, A, and AM, which contain retinotopic visual representations (Garrett et al., 2014; Wang and Burkhalter, 2007). By comparison, for neurons in primary visual cortex there was better agreement between responses seen in open-loop and during the task (Suppl. Figure 4**b**).

To assess the role of motor factors, similarly, we evaluated a model where PPC activity depends on the mouse's movement, measured by the ball's angular and linear velocities. These quantities are related to the derivatives of position z and heading θ, but they are not identical because they are in

bioRxiv preprint doi: https://doi.org/10.1101/166413; this version posted July 21, 2017. The copyright holder for this preprint (which was not certified by peer review) is the author/funder, who has granted bioRxiv a license to display the preprint in perpetuity. It is made available under aCC-BY-NC-ND 4.0 International license.

mouse-centered coordinates and are unconstrained by the boundaries of the virtual corridor. The model based on motor factors performed markedly worse than the model based on position and heading in virtual reality (Suppl. Figure 5).

Discussion

The literature on posterior parietal cortex (PPC) supports two distinct views of this region's function. One view sees it involved in body movement and navigation. The other sees PPC as involved in making decisions, especially those based on vision. Different studies assessed these views one at a time, but typically stopped short of acknowledging the other view, let alone pitching the two views against the other.

To evaluate and potentially combine these views, we used a virtual reality task where animals use vision to decide and navigate. Our results resonate with the view that rodent PPC encodes combinations of spatial attributes (McNaughton et al., 1994; Nitz, 2006, 2012; Save and Poucet, 2000, 2009; Whitlock et al., 2012; Wilber et al., 2014). Specifically, we found that the activity of PPC neurons can be accurately predicted based on two extremely simple spatial measures: position of the animal along the corridor, and heading direction. Using only these quantities we could predict PPC activity highly accurately, during a complex task involving body movement, vision, decision, and navigation. These predictions are superior to those based purely on vision or on body movement, and were not improved by taking into account the animal's decision.

Our results are fully consistent with the observation that PPC cells can be divided into groups forming distinct sequences of activations depending on upcoming choice (Harvey et al., 2012). However, in our data, this division into choice-dependent sequences, and indeed the sequences themselves, could be explained by the effect on PPC of two measurable factors: the physical trajectories taken by the mouse in different trials, and the preferences of different cells for different combinations of position and heading. The selectivity of PPC cells for heading and position fully explained their apparent selectivity for the mouse's decision.

Our results therefore appear to support a different view of PPC function to that proposed by Harvey et al (2012). We can see two possible explanations for this discrepancy. The first is a difference between the tasks: for example in our task, unlike Harvey et al's, the spatial cues indicating appropriate decision were visible until the end of the corridor. This might have caused the animals to employ different neural strategies, resulting in genuinely different types of PPC coding between the tasks.

A second possible explanation, however, is that the same combination of spatial factors can also explain the results of Harvey et al. (2012). Indeed, the mice in that study did exhibit differences in heading direction that correlated with the final decision, but the trials showing such differences were sequentially excluded from analysis until the difference in mean heading no longer reached statistical significance. After discarding these trials, the mean heading angle did not differ significantly between left- and right-choice trials by construction, but a correlation of mean lateral displacement and choice persisted. It would therefore be interesting to test whether spatial variables can explain the apparent decision-selectivity seen in Harvey et al's PPC recordings, for example using the methods employed here.

In conclusion, we found that the activity of neurons in posterior parietal cortex during a simple task involving movement, vision, decision, and navigation, can be accurately predicted based on the selectivity of the neurons for two spatial variables: the position of the mouse along the corridor, and its heading direction. Taking into consideration this selectivity, and the mouse behavior, explains the apparent formation of decision-dependent activity sequences in this task. In other words, when mice

bioRxiv preprint doi: https://doi.org/10.1101/166413; this version posted July 21, 2017. The copyright holder for this preprint (which was not certified by peer review) is the author/funder, who has granted bioRxiv a license to display the preprint in perpetuity. It is made available under aCC-BY-NC-ND 4.0 International license.

use vision to guide navigation, parietal cortex encodes navigational attributes such as position and heading rather than visual signals or abstract decisions.

Acknowledgments

We thank Charu Reddy for technical support. This work was supported by the European Research Council (project CORTEX), by the Simons Foundation (SCGB 325512), and by the Wellcome Trust (095668 and 095669). MC holds the GlaxoSmithKline / Fight for Sight Chair in Visual Neuroscience.

bioRxiv preprint doi: https://doi.org/10.1101/166413; this version posted July 21, 2017. The copyright holder for this preprint (which was not certified by peer review) is the author/funder, who has granted bioRxiv a license to display the preprint in perpetuity. It is made available under aCC-BY-NC-ND 4.0 International license.

Methods

All experimental procedures were conducted according to the UK Animals Scientific Procedures Act (1986). Experiments were performed at University College London, under personal and project licenses released by the Home Office following appropriate ethics review. We report here on experiments performed in 5 mice (two C57bl/6 mice and three Camk2a-tTA;Ai93(TITL-GCaMP6f);Emx1-IRES-Cre mice), of both sexes. Wild-type mice were acquired from The Jackson Laboratory (www.jax.org/strain/000664). Triple transgenic mice were bred by crossing Camk2a-tTA (www.jax.org/strain/007004), Ai93(TITL-GCaMP6f) (www.jax.org/strain/024103), and Emx1-IRES-Cre (www.jax.org/strain/005628).

Surgery

For the initial surgery the animal was anesthetized with isoflurane (Merial) at 5% for induction, and 0.75-1.5% during the surgery. Carprofen (5 mg/kg weight, Rimadyl, Pfizer) was administered SC for systemic analgesia, and dexamethasone (0.5 mg/kg weight, Colvasone, Norbrook) was administered as an anti-inflammatory agent to prevent brain swelling. The scalp was shaved and disinfected, and local analgesia (Lidocaine, 5% ointment, TEVA UK; or intradermal injection, 6mg/kg, Hameln Pharmaceuticals Ltd) was applied prior to the incision. The eyes were covered with eye-protective gel (Viscotears, Alcon; or Chloramphenicol, Martindale Pharmaceuticals Ltd). The animal was positioned in a stereotaxic frame (Lidocaine ointment was applied to the ear bars), the skin covering and surrounding the area of interest was removed, and the skull was cleaned of connective tissue. A custom headplate was positioned above the area of interest and attached to the bone with Superbond C&B (Sun Medical). Then, a round craniotomy (3-4 mm diameter) was made using fine-tipped diamond drill and/or a biopsy punch (Kai Medical). A cranial window was inserted into the craniotomy and fixed with Vetbond (3M) and Superbond C&B. The cranial window consisted of two superimposed round coverslips (WPI, #1 thickness) – one matching the inner diameter of the craniotomy (3-4 mm), and the other one providing mechanical support sitting on the skull (typically 5 mm diameter). The two coverslips were glued together beforehand using a Norland optical UV curing adhesive (NOA61, ThorLabs Inc.). After the surgery the animal was allowed to recover for three days before any behavioral or physiological measurements.

In case of C57Bl/6J mice, we injected the virus AAV2/1.Syn.GCaMP6f.WPRE.SV40 at a final concentration of 2.3e12 GC/ml before closing the craniotomy with the cranial window. 100 nl of the virus was injected 300 µm below the brain surface at each of two locations targeting PPC (AP = -2mm, ML = 1.7mm) and V1 (AP = -3.5mm, ML = 2.5mm). The virus was injected at a rate of 2.3 nl every 6 s (Nanoject II, Drummond). The injection pipette was kept in place for about 10 min after the end of the injection to allow full absorption of the virus solution in the tissue.

Widefield Imaging

To obtain maps of retinotopy we performed widefield imaging: fluorescence imaging on transgenic mice (GCaMP6f-TTA-Emx1-Cre), and intrinsic imaging on wildtype (C57bl6) mice, together with methods described previously (Garrett et al., 2014; Pisauro et al., 2013).

Water control

To motivate the mice to perform the behavioral task we controlled their water intake. Mice obtained a drop of water (typically 4 µl) for every correct choice. If the amount of water obtained during the task was inferior to a minimum daily dose (at least 40 ml/kg/day), the mice received the missing water through an appropriately weighted amount of Hydrogel. On rest days (typically Saturday and/or Sunday) the mice received all their water through Hydrogel.

bioRxiv preprint doi: https://doi.org/10.1101/166413; this version posted July 21, 2017. The copyright holder for this preprint (which was not certified by peer review) is the author/funder, who has granted bioRxiv a license to display the preprint in perpetuity. It is made available under aCC-BY-NC-ND 4.0 International license.

Virtual reality set up

The mouse was head fixed with a custom made headplate and the holder that does not obstruct the visual field of view. The mouse was free to run on an air-suspended Styrofoam ball (20 cm in diameter), the rotation of the ball was measured by two optical computer mice (Dombeck et al., 2010) and then used in the custom virtual reality engine implemented in Matlab utilizing OpenGL capabilities of Psychophysics Toolbox (Brainard, 1997; Pelli, 1997) to control the visual scene. The rotation component of the ball responsible for the mouse turning the virtual reality environment was presented on three computer monitors (Iiyama ProLite E1980SD, 1280x1024 pixels, 60 Hz) positioned in a U-shaped configuration around the mouse spanning 270 degrees of the visual field horizontally and 75 degrees vertically. We used a multiplex video card (Matrox TripleHead2Go Digital Edition) to present the visual stimulus on three monitors in a synchronized manner. The light intensity response of the green and the blue channels of the monitors was linearized, while the red component had been switched off to reduce light contamination in the fluorescence channel. In addition, to compensate for the light intensity drop-off at sharp viewing angles we attached three Fresnel lenses (f=22cm, BHPA220-2-6, Wuxi Bohai Optics Apparatus Electronic Co., Ltd, Wuxi, Jiangsu, China) in front of the monitors.

Behavior

In the virtual reality environment, a vertical grating appeared on the left or right wall of the corridor. The sequence of contrast values was randomly drawn from a uniform distribution, with negative values indicating positions on the left wall, and positive values positions on the right wall. However, to prevent the animal from developing behavioral bias, trials ending in a wrong choice were repeated until finished correctly, and the next trial in the sequence was again a random trial. Correct trials were indicated by a brief beep (0.1 s, 6.6 kHz) tone, while error trials were indicated by a brief (0.2 s) white noise sound. During the inter-trial interval (~2 s) the screen was gray. Trials not finished within 45 s were timed out and a longer (3 s) white-noise sound was played to the animal. Mice typically performed between 200 and 400 trials per session (session duration 45-60 minutes). The behavioral session was aborted when either the animal stopped performing, or stopped drinking the water reward.

Open loop

Open loop trials were run immediately after the actual behavioral session ('closed loop') recording the same cells. The water spout was removed, and the visual stimulus was constructed by chopping the 'closed loop' visual stimuli into 0.5 s segments and presenting them to the animal in randomized order. To reduce the flickering effect of the visual stimulus, each 0.5 s segment was modified by sinusoidally modulating the contrast at the frequency of 2 Hz, making the transition between the two sequential smooth. During the 'open loop' experiments the animal was free to run on the ball, however this was not affecting the visual stimuli presented. Typically, during these measurements the animals chose to alternate bouts of running with periods of rest.

Two-photon Imaging

Two-photon imaging was performed using a standard resonant B-Scope microscope (ThorLabs Inc.) equipped with Nikon 16x, 0.8 NA objective, and controlled by ScanImage 4.2 (Pologruto et al., 2003). Frame rate was set to ~30Hz, with the field of view of ~500x500 µm (512x512 pixels). This frame rate was further shared between 3-5 imaging planes spanning the depth of L2/3 using a piezo focusing device (P-725.4CA PIFOC, Physik Instrumente) resulting in a 6-10 Hz effective sampling rate per cell. Laser power was depth-adjusted and synchronized with piezo position using an electro-optical modulator (M350-80LA, Conoptics Inc.). The imaging objective and the piezo device were light shielded using a custom-made metal cone, a tube, and black cloth to prevent contamination of

bioRxiv preprint doi: https://doi.org/10.1101/166413; this version posted July 21, 2017. The copyright holder for this preprint (which was not certified by peer review) is the author/funder, who has granted bioRxiv a license to display the preprint in perpetuity. It is made available under aCC-BY-NC-ND 4.0 International license.

the fluorescent signal caused by the monitors' light. Excitation light at 970 nm was delivered by an Ultra II femtosecond laser (Coherent, UK)

Data preprocessing

Preprocessing of the two-photon data routinely included registration, segmentation, and neuropil correction. The whole cell detection pipeline is explained in Pachitariu et al. (2016). In addition, for the analysis of open-loop experiments we also applied a deconvolution algorithm to extract spikes from the continuous calcium data (Vogelstein et al., 2010). To calculate ΔF/F , the baseline fluorescence F_0 was taken as a 20th percentile of the overall level of fluorescence of a cell.

Estimation of z-θ maps

To estimate the position-heading field of each neuron we used a local likelihood approach (Loader, 1999). First, we used the data to estimate the occupancy map $M_{occ}(z,\theta)$ and the accumulated fluorescence signal map $M_{sig}(z,\theta)$. Then, we filtered both maps with a Gaussian filter, and we calculated the resulting position-heading map as:

$$F(z,\theta) = \frac{M_{sig}^{filt}(z,\theta) + \lambda \cdot F_{mean}}{M_{occ}^{filt}(z,\theta) + \lambda}$$

Where F_{mean} is the mean fluorescence of the cell, and λ is a small number used for regularization, to prevent large estimation errors in location where little or no data is available in z-θ space.

The size of the Gaussian filter $\{\sigma_z, \sigma_\theta\}$ was optimally chosen for each cell through a 10-fold cross-validation procedure. In this procedure, for each set of values $\{\sigma_z, \sigma_\theta\}$ 90% percent of the trials were chosen to estimate $\hat{F}(z,\theta)$. Then, performance of the model $\hat{F}(z,\theta)$ was measured on the remaining 10% of the trials. The procedure was repeated 10 times for different 90/10% partitioning of the data. The set of values $\{\sigma_z, \sigma_\theta\}$, which resulted in the best overall performance of the model was chosen as the optimal and further used in consequent analyses for that neuron.

Analysis of the open-loop data

Calcium dynamics measured with GCaMP6f is slow with decay times as long as a few hundreds of milliseconds (Chen et al., 2013). With the visual stimuli being 0.5s long and presented in randomized order this issue will cross-contaminate responses to sequential stimuli. For the analysis of the replay experiment, where this issue is critical, we have used inferred firing rate (Vogelstein et al., 2010) and not ΔF/F. To compare activity between the two conditions at the corresponding 0.5 s segments, we have used a correlation coefficient between the inferred firing rates (binned at 0.5 s) as a measure of similarity.

Decoding of population responses

To predict the distribution of locations in z-θ space visited by the animal during the session ($Pr(z,\theta)$) we used the position-heading maps ($\mu_i(z,\theta)$ estimated separately for each cell i), and employed a Bayesian approach.

Below we show that in this approach, the posterior probability distribution for the animal's position in z-θ space at time t is:

$$logPost(z,\theta) = -\sum_i \frac{\left(\mu_i(z,\theta) - r_i(t)\right)^2}{2\sigma_i^2} + logPr(z,\theta) + const$$

where $r_i(t)$ is the response of cell i at time t, and σ_i^2 is the overall variance of the response of cell i throughout the session.

To see this, assume that the response ($\Delta F/F$, or even simply F) of cell i at each location (z,θ) is a Gaussian random variable:

$$R_i(z,\theta) \sim N\left(\mu_i(z,\theta), \sigma_i(z,\theta)\right)$$

where $\mu_i(z,\theta)$ is the expected fluorescence of the cell at position (z,θ), i.e. its position-heading field, and $\sigma_i(z,\theta)$ is the variability of fluorescence at this location. Let's make the additional assumption that $\sigma_i(z,\theta) = \sigma_i$, i.e. it depends on the cell i but not on location in (z,θ).

bioRxiv preprint doi: https://doi.org/10.1101/166413; this version posted July 21, 2017. The copyright holder for this preprint (which was not certified by peer review) is the author/funder, who has granted bioRxiv a license to display the preprint in perpetuity. It is made available under aCC-BY-NC-ND 4.0 International license.

Given these assumptions, the probability of this random variable to equal the value r_i at time t is:

$$Pr\big(R_i(z,\theta) = r_i(t)\big) = \frac{1}{\sqrt{2\pi}\cdot\sigma_i} \cdot \exp\left(-\frac{\big(\mu_i(z,\theta) - r_i(t)\big)^2}{2\sigma_i^2}\right)$$

and the likelihood of a measured population response is:

$$L(z,\theta) = \prod_i Pr\big(R_i(z,\theta) = r_i(t)\big) = \prod_i \frac{1}{\sqrt{2\pi}\cdot\sigma_i} \cdot \exp\left(-\frac{\big(\mu_i(z,\theta) - r_i(t)\big)^2}{2\sigma_i^2}\right)$$

Taking the logarithm yields:

$$logL(z,\theta) = -\sum_i \frac{\big(\mu_i(z,\theta) - r_i(t)\big)^2}{2\sigma_i^2} - \sum_i \log(\sigma_i) - \sum_i \log\big(\sqrt{2\pi}\big)$$

If we want to incorporate the position prior (occupancy map) to get the *posterior* probability distribution:

$$Post(z,\theta) = L(z,\theta)\cdot Pr(z,\theta)$$

$$logPost(z,\theta) = logL(z,\theta) + logPr(z,\theta) = -\sum_i \frac{\big(\mu_i(z,\theta) - r_i(t)\big)^2}{2\sigma_i^2} - \sum_i \log(\sigma_i) - \sum_i \log\big(\sqrt{2\pi}\big) + logPr(z,\theta)$$

Dropping the constants leaves only position-dependent variables, to obtain the expression at the beginning of this section.

References

Andersen, R.A., and Buneo, C.A. (2002). Intentional maps in posterior parietal cortex. Annu Rev Neurosci 25, 189-220.

Andersen, R.A., and Cui, H. (2009). Intention, action planning, and decision making in parietal-frontal circuits. Neuron 63, 568-583.

Andersen, R.A., and Mountcastle, V.B. (1983). The influence of the angle of gaze upon the excitability of the light-sensitive neurons of the posterior parietal cortex. Journal Of Neuroscience 3, 532-548.

Bisley, J.W., and Goldberg, M.E. (2010). Attention, intention, and priority in the parietal lobe. Annu Rev Neurosci 33, 1-21.

Brainard, D.H. (1997). The Psychophysics Toolbox. Spatial Vision 10, 433-436.

Chen, T.W., Wardill, T.J., Sun, Y., Pulver, S.R., Renninger, S.L., Baohan, A., Schreiter, E.R., Kerr, R.A., Orger, M.B., Jayaraman, V., *et al.* (2013). Ultrasensitive fluorescent proteins for imaging neuronal activity. Nature 499, 295-300.

Cohen, Y.E., and Andersen, R.A. (2002). A common reference frame for movement plans in the posterior parietal cortex. Nat Rev Neurosci 3, 553-562.

Dombeck, D.A., Harvey, C.D., Tian, L., Looger, L.L., and Tank, D.W. (2010). Functional imaging of hippocampal place cells at cellular resolution during virtual navigation. Nat Neurosci 13, 1433-1440.

Erlich, J.C., Brunton, B.W., Duan, C.A., Hanks, T.D., and Brody, C.D. (2015). Distinct effects of prefrontal and parietal cortex inactivations on an accumulation of evidence task in the rat. Elife 4.

Garrett, M.E., Nauhaus, I., Marshel, J.H., and Callaway, E.M. (2014). Topography and areal organization of mouse visual cortex. Journal Of Neuroscience 34, 12587-12600.

Goard, M.J., Pho, G.N., Woodson, J., and Sur, M. (2016). Distinct roles of visual, parietal, and frontal motor cortices in memory-guided sensorimotor decisions. Elife 5.

Gold, J.I., and Shadlen, M.N. (2007). The neural basis of decision making. Annu Rev Neurosci 30, 535-574.

Harvey, C.D., Coen, P., and Tank, D.W. (2012). Choice-specific sequences in parietal cortex during a virtual-navigation decision task. Nature 484, 62-68.

bioRxiv preprint doi: https://doi.org/10.1101/166413; this version posted July 21, 2017. The copyright holder for this preprint (which was not certified by peer review) is the author/funder, who has granted bioRxiv a license to display the preprint in perpetuity. It is made available under aCC-BY-NC-ND 4.0 International license.

Katz, L.N., Yates, J.L., Pillow, J.W., and Huk, A.C. (2016). Dissociated functional significance of decision-related activity in the primate dorsal stream. Nature.

Kirkcaldie, M.T.K. (2012). Neocortex. In The Mouse Nervous System, C. Watson, G. Paxinos, and L. Puelles, eds. (Academic Press), pp. 52-111.

Latimer, K.W., Yates, J.L., Meister, M.L., Huk, A.C., and Pillow, J.W. (2015). Single-trial spike trains in parietal cortex reveal discrete steps during decision-making. Science 349, 184-187.

Licata, A.M., Kaufman, M.T., Raposo, D., Ryan, M.B., Sheppard, J.P., and Churchland, A.K. (2017). Posterior Parietal Cortex Guides Visual Decisions in Rats. Journal Of Neuroscience 37, 4954-4966.

Loader, C. (1999). Local Regression and Likelihood (Springer, New York).

McNaughton, B.L., Mizumori, S.J., Barnes, C.A., Leonard, B.J., Marquis, M., and Green, E.J. (1994). Cortical representation of motion during unrestrained spatial navigation in the rat. Cereb Cortex 4, 27-39.

Milner, A.D., and Goodale, M.A. (2006). The visual brain in action, 2nd edn (Oxford University Press).

Nitz, D.A. (2006). Tracking route progression in the posterior parietal cortex. Neuron 49, 747-756.

Nitz, D.A. (2012). Spaces within spaces: rat parietal cortex neurons register position across three reference frames. Nat Neurosci 15, 1365-1367.

Oram, M.W., Foldiak, P.F., Perrett, D.I., and Sengpiel, F. (1998). The "ideal homunculus": decoding neural population signals. Trends in Neurosciences 21, 259-265.

Pachitariu, M., Stringer, C., Schroeder, S., Rossi, L.F., Dipoppa, M., Carandini, M., and Harris, K.D. (2016). Suite2p: beyond 10,000 neurons with standard two-photon microscopy. bioRxiv.

Park, I.M., Meister, M.L., Huk, A.C., and Pillow, J.W. (2014). Encoding and decoding in parietal cortex during sensorimotor decision-making. Nat Neurosci 17, 1395-1403.

Pelli, D.G. (1997). The VideoToolbox software for visual psychophysics: Transforming numbers into movies. Spatial Vision 10, 437-442.

Pisauro, M.A., Dhruv, N.T., Carandini, M., and Benucci, A. (2013). Fast hemodynamic responses in the visual cortex of the awake mouse. Journal Of Neuroscience 33, 18343-18351.

Platt, M.L., and Glimcher, P.W. (1999). Neural correlates of decision variables in parietal cortex. Nature 400, 233-238.

Pologruto, T.A., Sabatini, B.L., and Svoboda, K. (2003). ScanImage: flexible software for operating laser scanning microscopes. Biomed Eng Online 2, 13.

Raposo, D., Kaufman, M.T., and Churchland, A.K. (2014). A category-free neural population supports evolving demands during decision-making. Nat Neurosci.

Save, E., and Poucet, B. (2000). Hippocampal-parietal cortical interactions in spatial cognition. Hippocampus 10, 491-499.

Save, E., and Poucet, B. (2009). Role of the parietal cortex in long-term representation of spatial information in the rat. Neurobiology of learning and memory 91, 172-178.

Sugrue, L.P., Corrado, G.S., and Newsome, W.T. (2004). Matching behavior and the representation of value in the parietal cortex. Science 304, 1782-1787.

Vogelstein, J.T., Packer, A.M., Machado, T.A., Sippy, T., Babadi, B., Yuste, R., and Paninski, L. (2010). Fast nonnegative deconvolution for spike train inference from population calcium imaging. J Neurophysiol 104, 3691-3704.

Wang, Q., and Burkhalter, A. (2007). Area map of mouse visual cortex. The Journal of comparative neurology 502, 339-357.

Whitlock, J.R. (2014). Navigating actions through the rodent parietal cortex. Frontiers in human neuroscience 8, 293.

Whitlock, J.R., Pfuhl, G., Dagslott, N., Moser, M.B., and Moser, E.I. (2012). Functional split between parietal and entorhinal cortices in the rat. Neuron 73, 789-802.

Wilber, A.A., Clark, B.J., Forster, T.C., Tatsuno, M., and McNaughton, B.L. (2014). Interaction of egocentric and world-centered reference frames in the rat posterior parietal cortex. Journal Of Neuroscience 34, 5431-5446.

Zhang, K., Ginzburg, I., McNaughton, B.L., and Sejnowski, T.J. (1998). Interpreting neuronal population activity by reconstruction: unified framework with application to hippocampal place cells. J Neurophysiol 79, 1017-1044.

Zhuang, J., Ng, L., Williams, D., Valley, M., Li, Y., Garrett, M., and Waters, J. (2017). An extended retinotopic map of mouse cortex. Elife 6.

bioRxiv preprint doi: https://doi.org/10.1101/166413; this version posted July 21, 2017. The copyright holder for this preprint (which was not certified by peer review) is the author/funder, who has granted bioRxiv a license to display the preprint in perpetuity. It is made available under aCC-BY-NC-ND 4.0 International license.

Figures

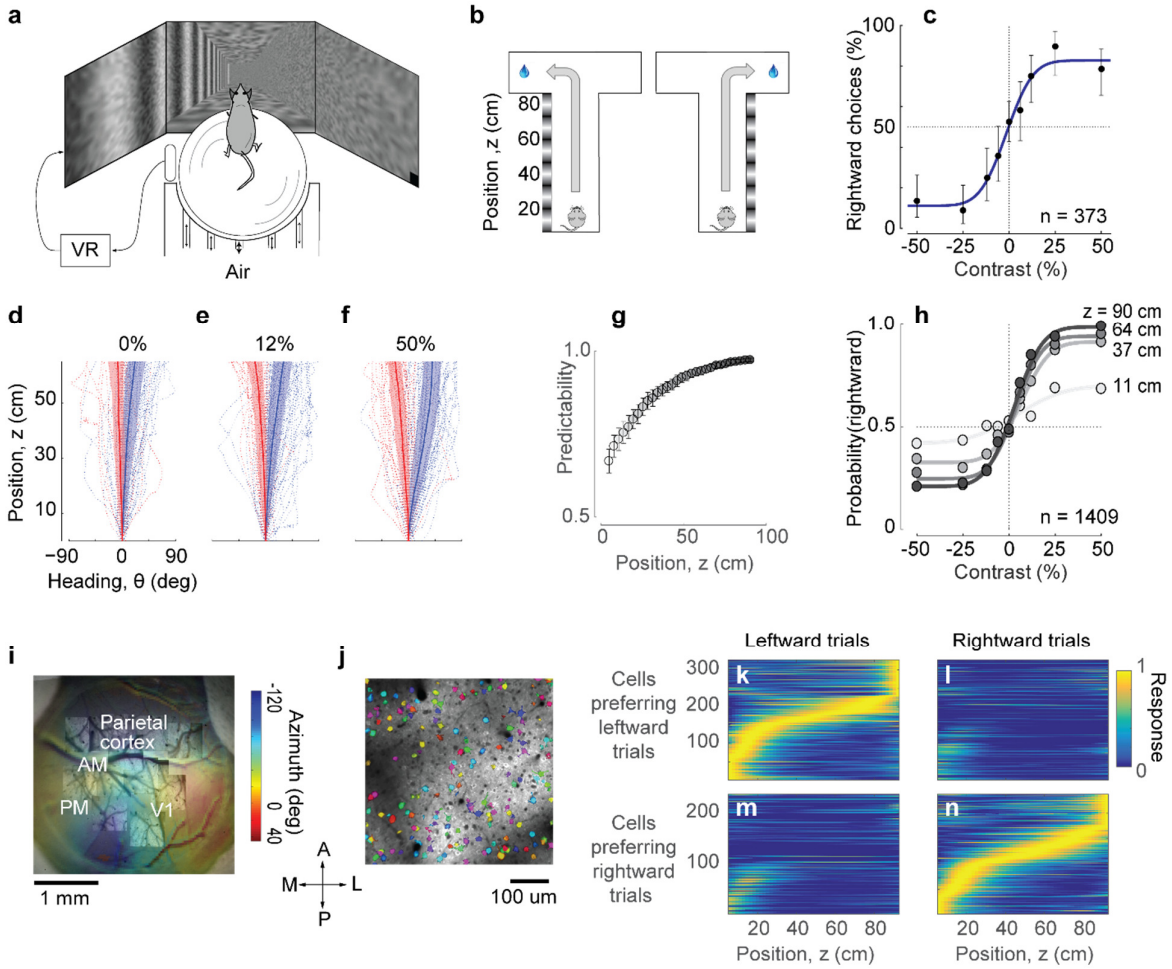

Figure 1. Imaging PPC activity during a task probing vision, decision, and navigation. **a**. Schematic view of the experimental setup from behind the mouse. The monitors are positioned at 90 degrees relative to each other, spanning 270 degrees of the horizontal field of view of the mouse. **b**. Schematic view of the virtual environment. The mouse receives a drop of water reward once it gets into the correct arm of the T-maze. A brief white noise sound is played if the choice is wrong. **c**: Example single session psychometric curve. Negative values of contrast indicate stimuli on the left wall, positive values indicate stimuli on the right wall. Error bars indicate 95% confidence intervals. **d-f**: Examples of trajectories in position-heading coordinates within a single training session. For easier trials (gratings with higher contrast), the trajectories tended to diverge sooner, while for the zero-contrast trials (**d**) the trajectories diverged only towards the end of the corridor. **g**. Predicting the final choice of the animal by observing its heading at different stages of the task (error bars represent s.e.m.). Predictability (i.e. the probability of a correct prediction) becomes larger as the animal progresses through the maze. **h**. Psychometric functions produced by heading-based prediction of the animal's choice. From being almost flat in the beginning of the maze, the curves evolve as the animal progresses through the task (levels of gray correspond to position z as in **g**). **i**. Retinotopic map acquired using widefield imaging of a GCaMP6f transgenic mouse. This map is used in combination with stereotaxic coordinates to identify brain areas. **j**. A mean fluorescence image of a single plane after image registration. Active cells, as detected from the two-photon imaging data, are overlaid over the mean image. Different cells are marked with a different hue. **k-n**. Choice-specific sequences of activity. Cells in PPC were selective to the trial outcome, and were also only active during a specific position in the T-Maze.

bioRxiv preprint doi: https://doi.org/10.1101/166413; this version posted July 21, 2017. The copyright holder for this preprint (which was not certified by peer review) is the author/funder, who has granted bioRxiv a license to display the preprint in perpetuity. It is made available under aCC-BY-NC-ND 4.0 International license.

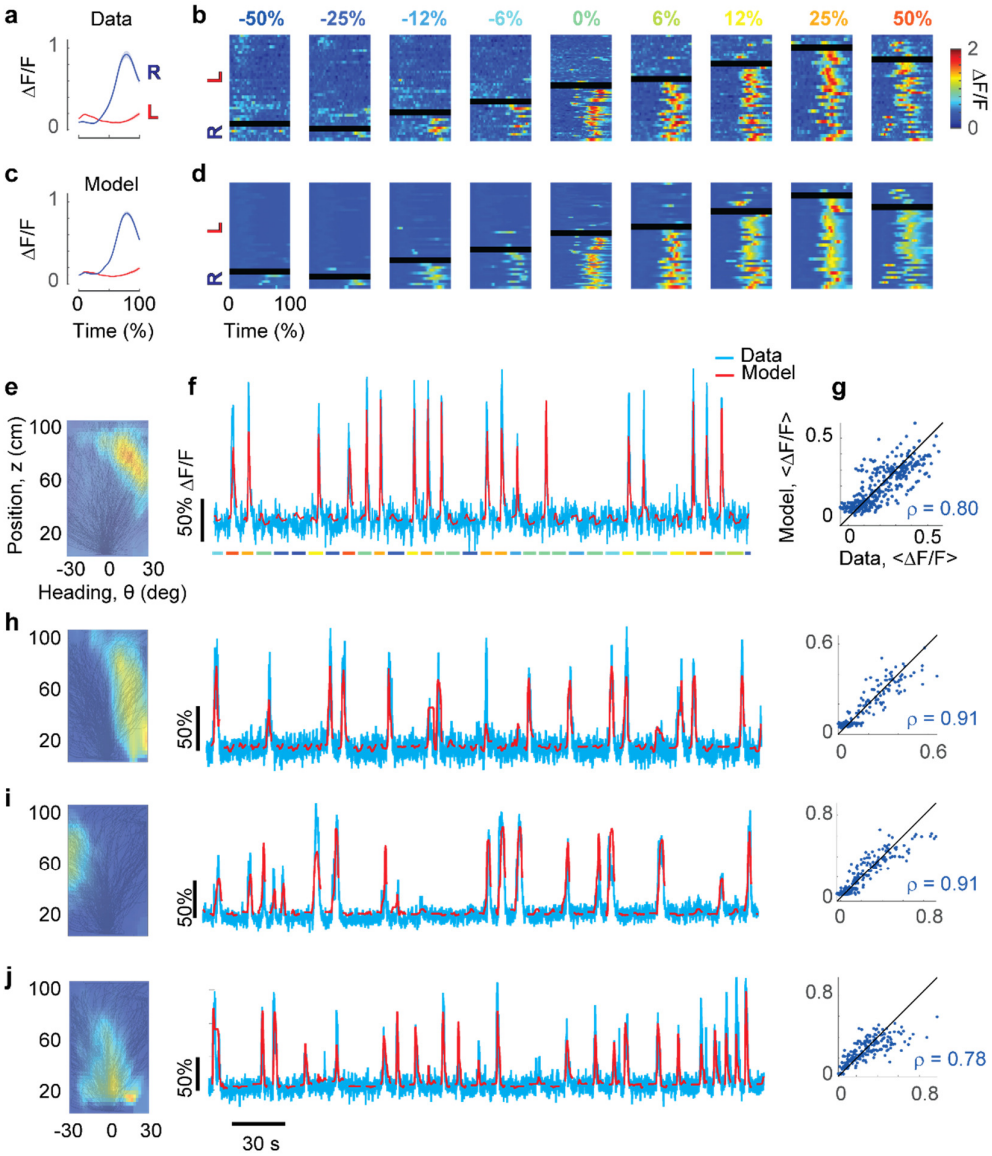

Figure 2. Predicting the responses of PPC neurons based on position and heading. **a.** Average response of an example neuron over trials that ended in rightward or leftward choice. **b.** Pseudocolor representation of the cell's activity during all individual trials in the session. Each panel corresponds to a single contrast, with all trials of this contrast arranged in rows. Trials ending in rightward vs. leftward choices are separated by a black bar. The traces are aligned to the beginning and the end of each trial. **c,d**. Same as in **a**, **b**, but calculated from the cell activity predicted by the position-heading model in **e**. **e**. Position-heading field of this example neuron. Color represents the normalized $\Delta F/F$ of the neuron. Black lines show the trajectories in z-θ space taken by the animal during the behavioral session. This example neuron was active towards the end of the corridor and while the mouse was heading to the right. **f**. Model prediction (*red*) compared to the actual calcium traces (*cyan*) in representative trials. Grating contrast of the current trial is color-coded by the dashed line below the traces (same color scheme as above plots in **b**). **g.** The model provides a good explanation for the different levels of activity of the cell in different trials, with a correlation between actual data and model prediction of 0.8. **h-j.** Examples of three other cells with position-heading fields in different locations.

bioRxiv preprint doi: https://doi.org/10.1101/166413; this version posted July 21, 2017. The copyright holder for this preprint (which was not certified by peer review) is the author/funder, who has granted bioRxiv a license to display the preprint in perpetuity. It is made available under aCC-BY-NC-ND 4.0 International license.

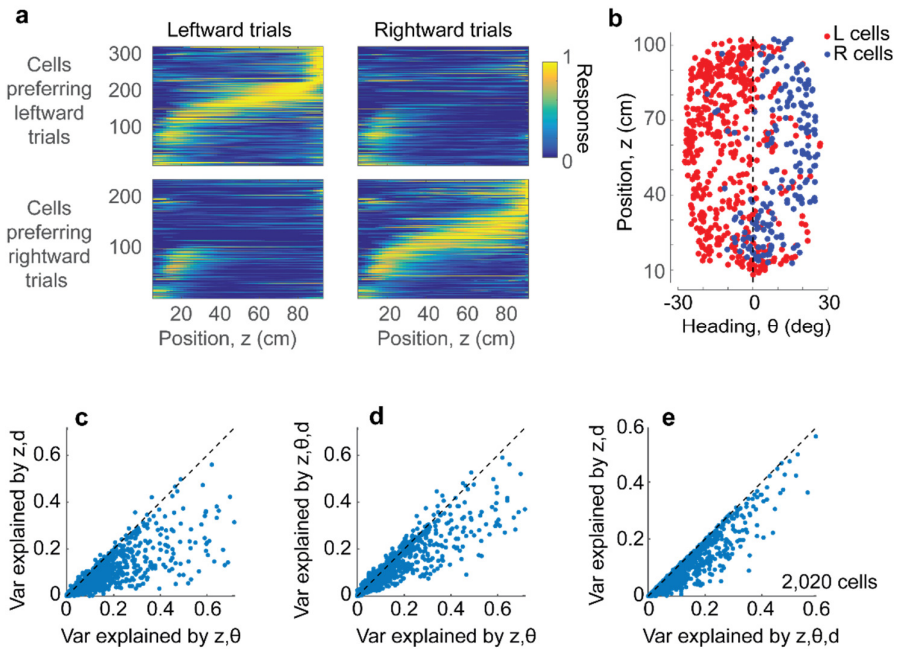

Figure 3. Position and heading are sufficient to explain the dependence of responses on choice. **a**. The position-heading model correctly predicts the sequential choice-selective activations seen in the data (compare to Figure 1**k-n**, where cells are arranged in the same order). **b**. The centers of the position-heading fields of all the cells, colored according to whether the cells fired preferentially in trials that ended in leftward (*red*) or rightward choices (*blue*). Almost invariably, the former group of cells preferred negative (leftward) heading angles, and the latter group of cells preferred positive (rightward) heading angles. **c**. Variance explained (cross-validated) by an alternative model based on position (z) and decision (d) (abscissa) vs the model based on position (z) and heading (θ) (ordinate). Each point indicates a cell measured in PPC (n = 2,020). The position-heading model clearly makes better predictions. As elsewhere in the paper, decision was defined as the final choice (report) made by the animal on that trial. **d.** Adding decision to the position-heading model does not improve predictions of PPC cell responses. The cross-validated explained variance of the model that uses z, θ, and decision is lower than that of the position-heading (z and θ) model. **e**. Accordingly, removing the heading θ from the full (z,θ,d) model results in a model with poor performance.

bioRxiv preprint doi: https://doi.org/10.1101/166413; this version posted July 21, 2017. The copyright holder for this preprint (which was not certified by peer review) is the author/funder, who has granted bioRxiv a license to display the preprint in perpetuity. It is made available under aCC-BY-NC-ND 4.0 International license.

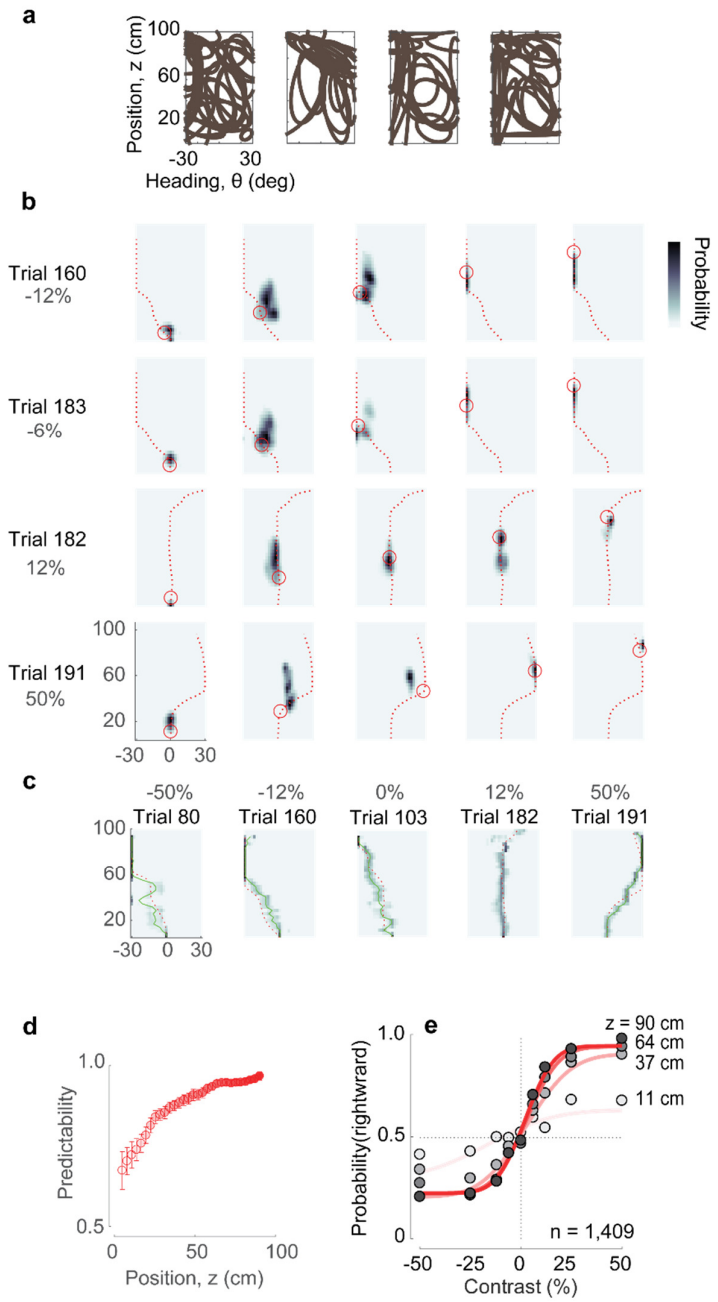

Figure 4. Decoding animal position and choice from neural activity. **a**. Outlines of position-heading fields of all neurons imaged in a session, for 4 sessions. **b**. The posterior estimate of the position closely follows the actual trajectory of the animal. Different rows represent different trials; different columns represent different moments in the trial. Red dashed line represents the trajectory of the mouse in the trial, circle – the actual position of the mouse in the T-maze. **c**. Estimated trajectories in z-θ space closely follow the actual trajectories of the mouse. The red dashed line represents the actual mouse's trajectory, green solid line represents estimated trajectory, superimposed on a pseudocolor representation of the underlying posterior probability distribution. **d**. Choice predictability, as estimated from the decoded trajectories at different stages of the task, from early in the task (faint red) to late in the task (full red). The neurometric choice predictability increases as the mouse progresses through the corridor, meaning that the final choice becomes increasingly more predictable from the neural activity. Error bars represent s.e.m. **e**. Neurometric functions, estimated at different positions in the corridor (faint red line to full red line). The data points here are the same as in Figure 1**h**, however the curves are fit to the data points decoded from neural activity (not shown).

bioRxiv preprint doi: https://doi.org/10.1101/166413; this version posted July 21, 2017. The copyright holder for this preprint (which was not certified by peer review) is the author/funder, who has granted bioRxiv a license to display the preprint in perpetuity. It is made available under aCC-BY-NC-ND 4.0 International license.

Supplementary Figures

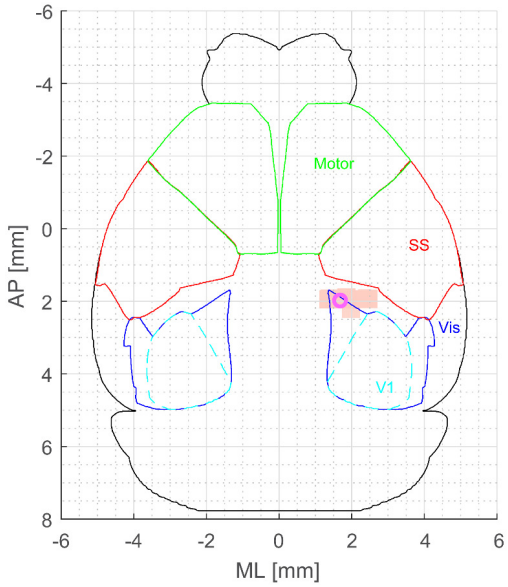

Suppl. Figure 1. Location of imaged neurons relative to somatosensory and primary visual cortices. Outlines of visual, primary visual, somatosensory and motor cortices were derived from Allen Institute atlas, and aligned to coordinates relative to bregma – [0, 0]. Magenta circle represents the coordinates of PPC as identified in Harvey et al. (2012) – [-2.0 AP, 1.7ML]. Peach-colored patch represents the FOVs of the two-photon imaging sessions.

bioRxiv preprint doi: https://doi.org/10.1101/166413; this version posted July 21, 2017. The copyright holder for this preprint (which was not certified by peer review) is the author/funder, who has granted bioRxiv a license to display the preprint in perpetuity. It is made available under aCC-BY-NC-ND 4.0 International license.

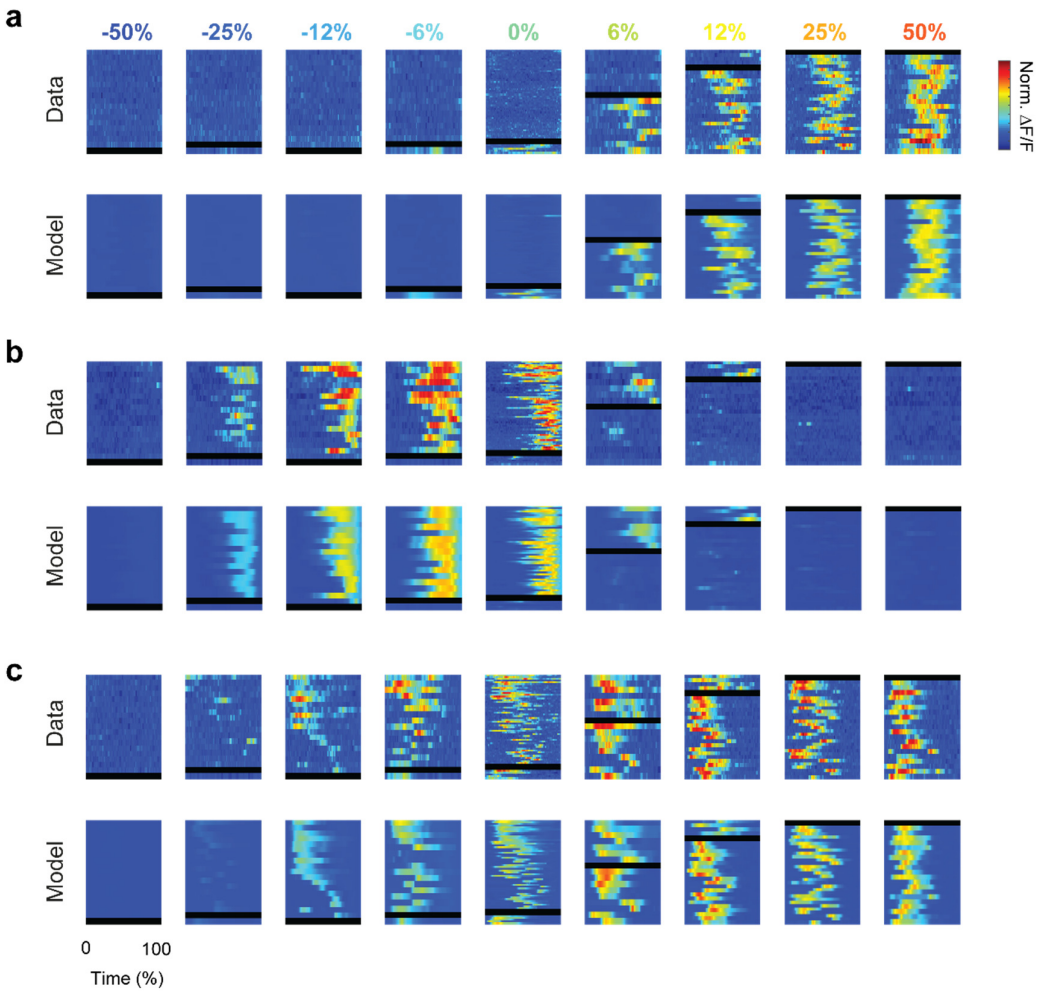

Suppl. Figure 2. Single-trial responses and model predictions for 3 example cells. **a**. Responses (top) and model predictions (bottom) for the cell in Figure 2**h**. Format as in Figure 2**b**,**d**. **b**,**c**: same as **a**, for the example cells in Figure 2**i**-**j**.

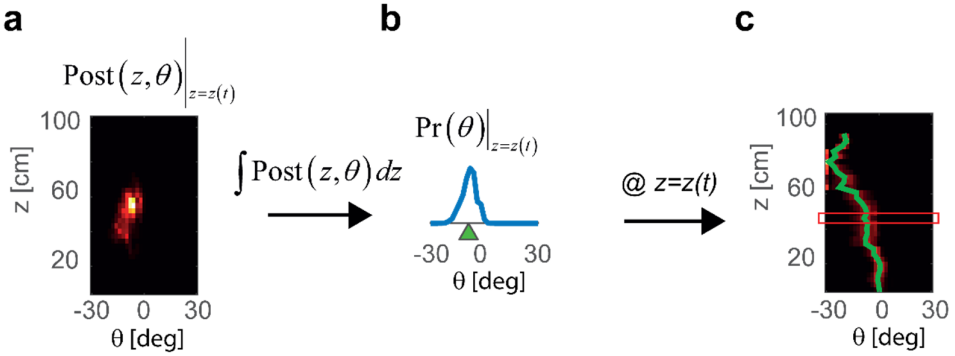

Suppl. Figure 3.Full trajectory decoding from a sequence of posterior distribution estimates. **a**. Posterior distribution estimated from PPC population activity at a specific time *t* and *z= z(t)*. **b**. Probability distribution of the heading angle $\Pr(\theta)$ is estimated by calculating an integral of the posterior distribution from **a** across z. Heading angle θ is estimated as a center of mass of $\Pr(\theta)$. **c**. Performing the steps in **a** and **b** for each *z* provides a prediction of the whole trajectory of the mouse during the trial (green line). Red frame indicates the *z=z(t)* from the example frame in **a** and **b**.

bioRxiv preprint doi: https://doi.org/10.1101/166413; this version posted July 21, 2017. The copyright holder for this preprint (which was not certified by peer review) is the author/funder, who has granted bioRxiv a license to display the preprint in perpetuity. It is made available under aCC-BY-NC-ND 4.0 International license.

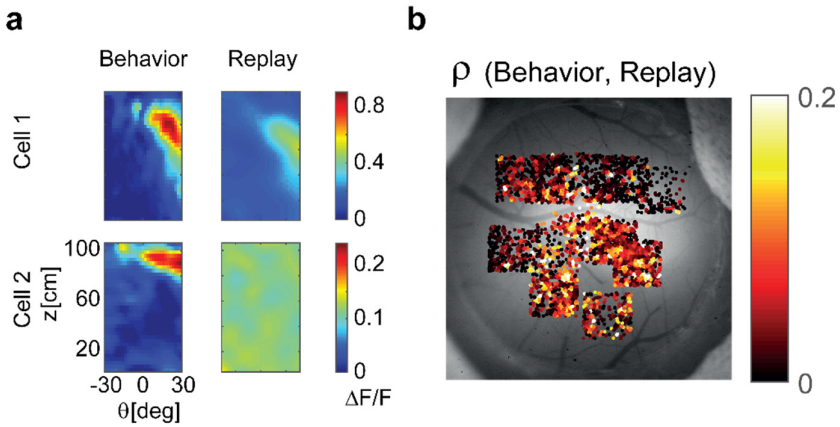

Suppl. Figure 4. Assessing the role of visual factors **a.** In the open loop condition, the estimated place-heading fields of PPC neurons were either much weaker (example cell 1) than during the closed-loop behavior, or completely absent (example cell 2) **b**. When comparing responses between open loop and closed loop, neurons in primary visual cortex showed more similarity in their responses between the two conditions than neurons in PPC.

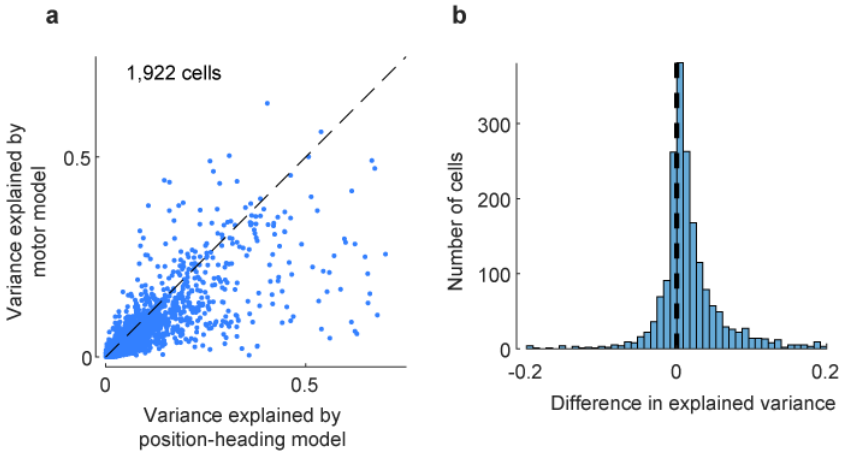

Suppl. Figure 5. Assessing the role of motor factors. **a**. The position-heading model performs better than the alternative motor model, as measured by cross-validated explained variance. **b**. The explained variance of the position-heading model is significantly larger than the explained variance of the motor model ($p<<0.001$, one-sided t-test).

Supplementary Movies

Suppl. Movie 1. A mouse performing a few trials of the task.

Suppl. Movie 2. Frame-by-frame decoding of mouse position from PPC population activity. The contrast used in each trial is indicated by the grating on one of the sides of the z-θ map. The trajectory of the mouse in the whole trial is indicated by a black dashed line, and the frame-by-frame position of the mouse is indicated by a circle. The color-coded map is the log posterior distribution of the current position of the mouse estimated from population activity of PPC neurons.